

www.acsnano.org

Anisotropic Disorder and Thermal Stability of Silicane

Bradley J. Ryan, Luke T. Roling,* and Matthew G. Panthani*



Cite This: ACS Nano 2021, 15, 14557-14569



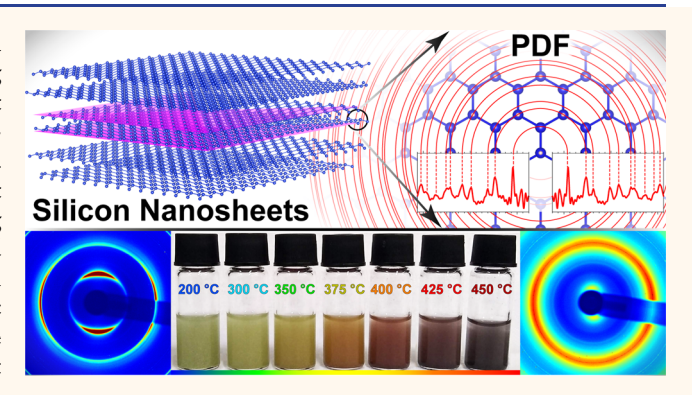
ACCESS I

Metrics & More

Article Recommendations

s Supporting Information

ABSTRACT: Atomically thin silicon nanosheets (SiNSs), such as silicane, have potential for next-generation computing paradigms, such as integrated photonics, owing to their efficient photoluminescence emission and complementary-metal-oxide-semiconductor (CMOS) compatibility. To be considered as a viable material for next-generation photonics, the SiNSs must retain their structural and optical properties at operating temperatures. However, the intersheet disorder of SiNSs and their nanoscale structure makes structural characterization difficult. Here, we use synchrotron X-ray diffraction and atomic pair distribution function (PDF) analysis to characterize the anisotropic disorder within SiNSs, demonstrating they exhibit disorder within the intersheet spacing, but have little transla-



tional or rotational disorder among adjacent SiNSs. Furthermore, we identify changes in their structural, chemical, and optical properties after being heated in an inert atmosphere up to 475 °C. We characterized changes of the annealed SiNSs using synchrotron-based total X-ray scattering, infrared spectroscopy, X-ray photoelectron spectroscopy, scanning electron microscopy, electron paramagnetic resonance, absorbance, photoluminescence, and excited-state lifetime. We find that the silicon framework is robust, with an onset of amorphization at ~ 300 °C, which is well above the required operating temperatures of photonic devices. Above ~ 300 °C, we demonstrate that the SiNSs begin to coalesce while keeping their translational alignment to yield amorphous silicon nanosheets. In addition, our DFT results provide information on the structure, energetics, band structures, and vibrational properties of 11 distinct oxygen-containing SiNSs. Overall, these results provide critical information for the implementation of atomically thin silicon nanosheets in next-generation CMOS-compatible integrated photonic devices.

KEYWORDS: silicon nanosheets, pair distribution function, photonics, optoelectronic, density functional theory

wo-dimensional (2D) materials have recently gained interest for their potential in applications such as photodetectors, 1-3 energy storage, 4-7 photovoltaics, 8 and as quantum materials. 9-11 Among the 2D materials, atomically thin hydrogen-terminated silicon nanosheetsoften referred to as "silicane"—have garnered attention due to their optical properties, showing potential for direct bandgap-like behavior in a form of silicon, which has been a long-standing goal in the fields of materials science and computing. Atomically thin silicon (111) nanosheets (SiNSs) are interesting in their own right as an optoelectronic material, but the applicability of any gained knowledge of SiNSs provides additional value to the scientific community, as it also provides a deeper level of understanding for all silicon-based systems. These SiNSs are atomically thin, represent an isolated silicon surface, and can serve as a model system for understanding the chemistry and properties of other silicon-

based systems. Thus, SiNSs represent an interesting material system that is in its infancy of our understanding.

To fully understand the origin of the light-emitting properties of SiNSs, an atomic-level understanding of the structure is required. However, the substantial disorder in the intersheet spacing and their nanoscale structure makes conventional X-ray diffraction difficult.¹² Previously, we determined the local structure of the SiNSs to consist of an atomically thin silicon (111) backbone arranged in a buckled-honeycomb pattern; we found that the silicon atoms are primarily terminated with monohydrides, with an approximate

Received: May 18, 2021 Accepted: August 30, 2021 Published: September 10, 2021





chemical formula of $SiH_{0.8}O_{0.1}Cl_{0.1}$. ¹² However, our prior study only probed local coordination and bonding, motivating the study of the extended structure.

Another important factor in determining the viability of materials for computing is their thermal stability. Semi-conductor-based electronic devices used in industrial, commercial, and military applications commonly require operability up to 125 °C. 13,14 Thus, to assess the feasibility of using SiNSs in computing applications, we sought to characterize the thermal stability and optical properties of the SiNSs after exposing them to a range of elevated temperatures.

To obtain a more complete description of the long-range structure of SiNSs and to evaluate their stability upon exposure to elevated temperatures, we used atomic pair distribution function (PDF) analysis derived from synchrotron-based total X-ray scattering obtained at beamline 11-ID-B at the Argonne National Laboratory Advanced Photon Source. PDF analysis can obtain an atomic-level understanding of materials that do not contain long-range periodicity, such as nanomaterials. 15-1 Importantly, PDFs can be used to refine structural models, similar to Rietveld refinement¹⁹ in conventional X-ray diffraction. Periodic crystalline materials yield PDFs with sharp peaks with relatively little attenuation in intensity over a long range, while amorphous materials give rise to broad peaks whose intensity decays after a few angstroms. Each peak in the PDF corresponds to a pair of scattering atoms at a given distance, and the area of each peak is related to the number of scatterers at that distance.

Here, we present total X-ray scattering, synchrotron powder X-ray diffraction, and PDF analysis and confirm that the SiNSs consist of an atomically thin silicon backbone arranged in a buckled-honeycomb pattern. We find that the nanosheets have substantial disorder within the intersheet spacing, but on average retain the same translational alignment and stacking sequence as the CaSi₂ precursor. We investigate the thermal stability of the SiNSs; we find that the silicon framework comprising the SiNSs is structurally stable at temperatures less than ~300 °C. At temperatures greater than or equal to ~300 °C, the passivating hydrogen and chlorine atoms leave the surface of the SiNSs and Si-Si bonds are formed among adjacent nanosheets as the SiNSs coalesce to yield a product that is optically and structurally similar to amorphous silicon nanosheets by 425 °C. The optical properties are stable below ~200 °C, above which we observed a monotonic decrease in the photoluminescence intensity, photoluminescence quantum yield, and the excited-state lifetime. The photoluminescence is nearly completely quenched at annealing temperatures greater than ~375 °C. These results demonstrate that SiNSs are a viable CMOS-compatible optoelectronic material that is stable at the most stringent of operating temperatures.

RESULTS AND DISCUSSION

We previously determined that the local bonding and coordination of SiNSs are consistent with an atomically thin layer of hexagonally arranged Si atoms, with each Si atom connected to three other Si atoms and predominantly one hydrogen atom. Here, we sought to further elucidate the structure of SiNSs using atomic PDF analysis. While conventional X-ray diffraction (XRD) uses Bragg diffraction to characterize long-range periodicity, PDF uses total X-ray scattering to characterize structures that may not be periodic over long length scales. Description

The SiNS product obtained from deintercalation is a yellow fluffy powder whose volume is $\sim 150\%$ of the volume of the CaSi₂ precursor. Furthermore, the SiNSs do not form cohesive crystallites. Thus, this brings into question the stacking sequence and registry of adjacent sheets within stacks of SiNSs. The stacking sequence within disordered stacks of SiNSs has not been studied in the literature, which motivates performing structural refinement to elucidate the long-range structure. During the structural refinement process, we investigated several degrees of freedom, including the number of sheets within a unit cell, the spacing between sheets, the relative translational and rotational alignment of each sheet within the unit cell, and location of each atom within each sheet (Figure 1).

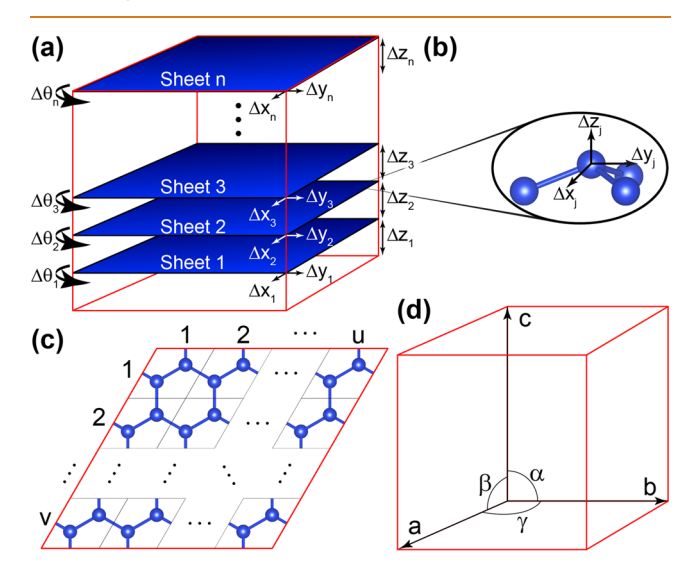


Figure 1. Illustrations depicting the degrees of freedom considered during the atomic PDF refinement of SiNSs. Unit cell boundaries are shown in red. All hydrogen atoms are omitted for clarity. (a) The translational and rotational degrees of freedom of n SiNSs relative to the unit cell: Δx_n , Δy_n , Δz_n , and $\Delta \theta_n$. (b) The degrees of freedom of an arbitrary j^{th} atom within a sheet: Δx_j , Δy_j , and Δz_j . (c) Lateral subunits contained within the $u \times v$ unit cell; each subunit is outlined with black lines. (d) Unit cell and its lattice parameters: a, b, c, α , β , γ .

Our initial attempts to refine the structure used the simplest unit cell possible: a single isolated SiNS where all degrees of freedom were refined. However, this model missed many features in the PDF (Figure S2). Similarly, we attempted to fit models that correspond to unit cells containing one, two, three, and four nanosheets, each yielding improvement to the fit. We ultimately deduced that a unit cell consisting of six nanosheets that retains the same number of sheets per unit cell, stacking sequence, and x- and y-coordinates of each Si atom as the 6R-CaSi₂ precursor (Figure 2) was most appropriate (and is justified in the following paragraphs), where the 6R phase of CaSi₂ consists of six Si sheets per unit cell with each sequential sheet exhibiting a 30° rotation and a $a \times (^1/_3)$ and $b \times (^2/_3)$ translational shift (Figure 2). We recognize that relaxing the x- and y-coordinates of the unit cell consisting of six sheets gives marginal improvements to the fit and that better fits could be obtained by including a larger number of sheets within the unit cell (e.g., 12 or 18), but it is important to note that additional degrees of freedom introduced into the model might not provide additional physical insight despite

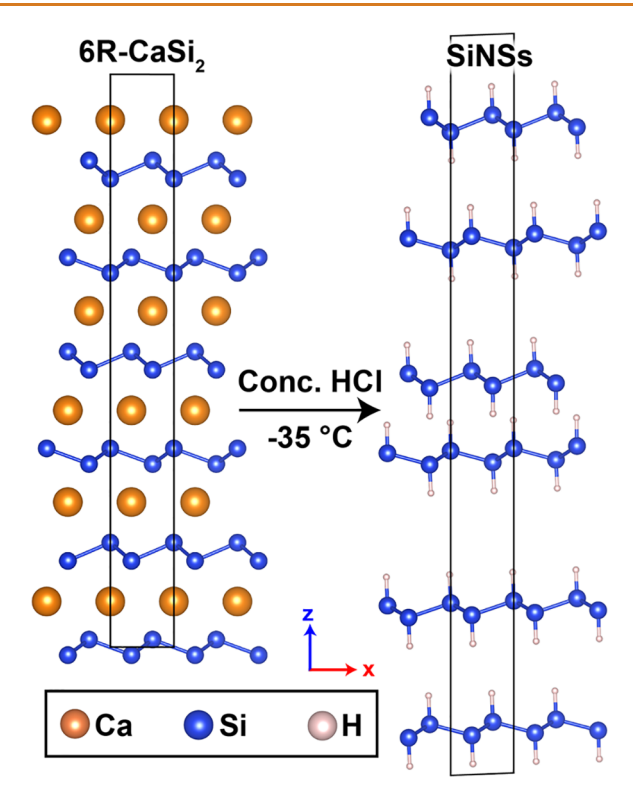


Figure 2. Schematic showing the 6R phase of CaSi₂ (left) and the refined structure of the SiNSs (right). The locations of the hydrogen atoms were determined by DFT. The black box corresponds to the unit cell.

improving the fit. Lastly, we would like to point out that we do not believe that the unit cell in Figure 2 corresponds to the "true" unit cell of the SiNSs, largely due to the inherent disorder within the sample, but we do believe that the presented unit cell does capture the structural characteristics of the experimental sample.

The refined structure consists of six SiNSs within a unit cell (Figure 2); however, we note that many peaks within the PDF align with a unit cell consisting of a single isolated SiNS without neighboring sheets (Figure 3a and Figure S2), albeit with a poor overall fit. This suggests that the features in PDF that are not captured by a single nanosheet are a result of small perturbations in the intersheet spacing of adjacent SiNSs along the c-axis. This is further supported by the broad (006) peak relative to the (110) and (100) peaks in the azimuthally integrated synchrotron powder X-ray diffraction data (AIspXRD) (Figure 3b). Further, we simulated the powder X-ray diffraction (pXRD) pattern of the refined structure containing six sheets per cell (Figure 3b), and upon comparing the simulated pXRD pattern to the AI-spXRD, we find that all of the low-intensity peaks in the simulated pXRD with Q < ~1 Å^{-1} correspond to lower-order (00*l*) peaks (with *l* < 6) that are not observed in the experimental data. These peaks with Q < $\sim 1 \text{ Å}^{-1}$ correspond to the m^{th} nearest neighboring sheets, for m ≥ 2 (note that m = n + 1 - l, for a unit cell containing nsheets). This indicates that stacking of individual SiNSs within the structure is not periodic. Rather, the lack of features at Q < \sim 1 Å⁻¹ and the broad (006) peak indicate a broad distribution of intersheet spacings centered at about 6.48 Å. To better model the intersheet disorder, we considered unit cells containing integer multiples of six sheets per unit cell (i.e., 12, 18, 24, ..., 48 sheets per unit cell) that again retain the same

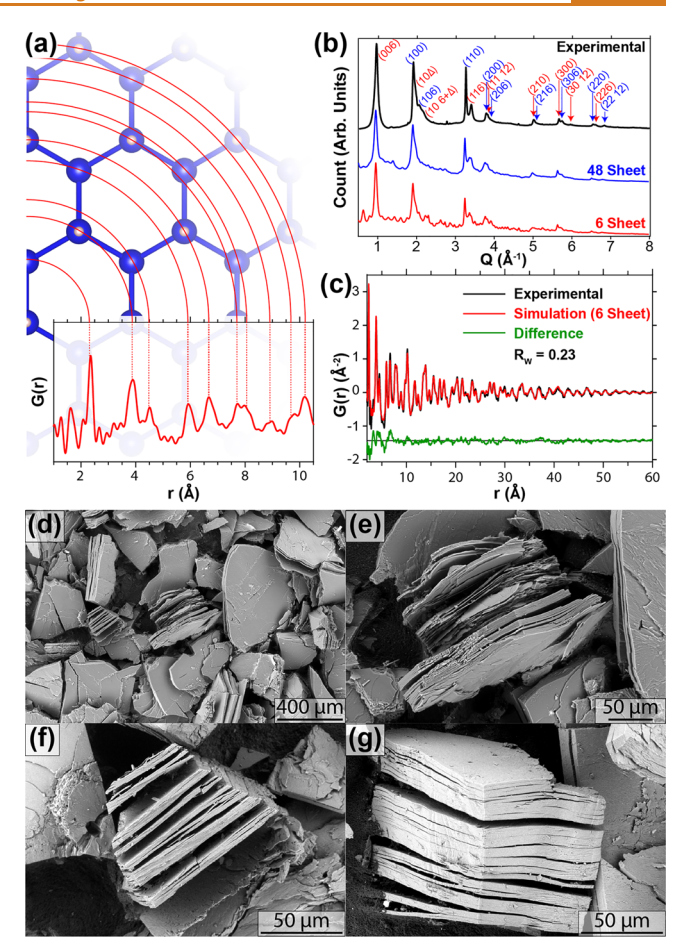


Figure 3. (a) Schematic of a single SiNS centered about an arbitrary Si atom, demonstrating each neighbor mapping onto each experimental PDF peak. (b) AI-spXRD of the unannealed experimental sample (top, black) and the simulated pXRD pattern for the refined structures (bottom, blue and red). The red and blue Miller indices are to help with differentiation. At $Q=\sim 2~\mathring{A}^{-1},~\Delta$ is an integer such that $1\leq\Delta\leq 5$. (c) Experimental PDF (black) and the refined 6-sheet structure (red) with the difference curve offset below (green). The AI-spXRD past $Q=\sim 6~\mathring{A}^{-1}$ shows an artificial decrease in intensity due to the edges of the detector. (d-g) SEM images of deintercalated SiNSs.

x- and y-coordinates and stacking sequence as 6R-CaSi₂, but the intersheet spacings were refined to the experimental PDF data. We find that the peaks at $Q < \sim 1 \text{ Å}^{-1}$ in the simulated pXRD are suppressed when modeling these larger unit cells (Figure 3b and S3); this supports that the peaks at $Q < \sim 1 \text{ Å}^{-1}$ in the simulated pXRD emerge from the periodicity of the simulated unit cell and are a result of modeling a disordered system with a periodic unit cell. In addition, the small, low-intensity ripples in the simulated pXRD (e.g., Q in the ranges of ca. 1.2–1.8, 2.5–3.2, and 4.0–4.9 Å⁻¹) are also suppressed when including increased sheets per unit cell (Figures 3b and S3), as these peaks also correspond to the periodicity of m^{th} nearest neighboring sheets (for $m \ge 2$) in the periodic unit cell.

The sharpest features within the experimental AI-spXRD (Figure 3b) arise from the (100) and (110) planes of the SiNSs. We find that the standard deviation in the *d*-spacing corresponding to the (110) plane is \sim 30 times less than that of the (006) plane. It is important to note that these planes intersect adjacent SiNSs (Figure S4). We find that the (100) peak at Q \approx 2 Å⁻¹ overlaps with many low-symmetry

reflections, giving it a broad appearance on the high-Q side of the peak and is discussed in the following paragraph. These observations further confirm that disorder arises from irregular intersheet spacing and excludes the possibility of substantial intersheet twisting or translational disorder in the x- or y-directions among neighboring sheets. Corroborating this observation, the 2D synchrotron powder X-ray diffraction data (2D-spXRD) (Figure 4 and Figure S5) show that the

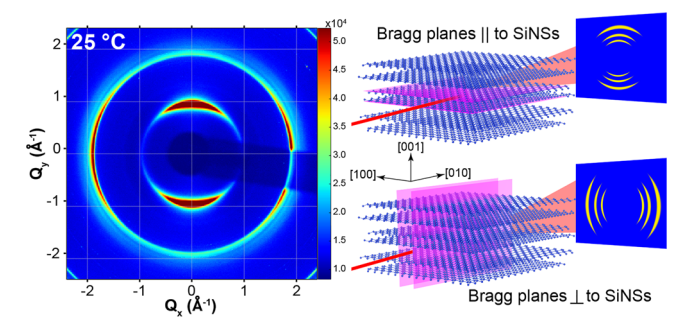


Figure 4. (Left) 2D-spXRD for the unannealed sample. (Right) Schematic demonstrating the relationship between peak location and SiNS orientation. On the top, the magenta planes illustrate the (006) planes; on the bottom, the magenta planes illustrate the (100) planes. The axis of the capillary would be parallel to the [001] direction. The incident X-ray is depicted in red.

(110) and (100) diffraction planes are predominantly oriented along $Q_Y = 0 \text{ Å}^{-1}$ (the horizontal axis), and the (006) reflection is strongest along the $Q_X = 0 \text{ Å}^{-1}$ direction (the vertical axis), indicating a preferential alignment of the SiNSs, with their normal vector oriented parallel to the axis of the capillary (consequently, perpendicular to the incident X-ray). The sharpness of the (100) and (110) peaks implies there is no substantial turbostratic twisting along the c-axis, nor translational disorder along the a- or b-axes. The absence of twisting and translational disorder supports our decision to fix the xand v-coordinates of the Si atoms within the aforementioned structural model to be the same as the CaSi₂ precursor. We believe that this long-range preferred orientation within the capillary arises from the process of packing the capillary itself, analogous to how playing cards align when dropped into a cylindrical tube (whose diameter is much larger than the lateral dimensions of the cards).²⁴ We do not see distinct hexagonally arranged diffraction reflections in the 2D-spXRD, which indicates that the SiNSs are, on average, not arranged with their normal vector aligned parallel to the X-rays; conversely, any sheets that are arranged with their normal vector parallel to the incident X-rays are randomly rotated about their normal vector such that they give rise to diffuse rings.

The peak at $Q \approx 2 \text{ Å}^{-1}$ primarily arises from the (100) plane; however, the high-Q side of this peak contains many features (Figure 3b). Given the aforementioned azimuthal dependence of the peaks corresponding to the (100), (110), and (006) planes, we examined the intensities of 12 wedges of the 2D-spXRD, comparing the relative intensities of the different peaks in each wedge (Figure S5). We determined that the peaks at $Q \approx 2 \text{ Å}^{-1}$ with $Q > Q_{(100)}$ have intensities that are inversely proportional to the (100) peak and are directly proportional to the (006) peak. This indicates that peaks on the high-Q side of the (100) peak have contributions from {10l}. Our assignment of these peaks is provided in Figure 3b. We find that the peaks centered at $Q = \sim 2 \text{ Å}^{-1}$ with $Q > Q_{(100)}$

arise from many sets of disordered planes; we grouped these broad peaks, and their indices are represented with a Δ , where Δ is an integer such that $1 \le \Delta \le 5$.

Regarding the PDF (Figure 3c), we find that refining the structure with a unit cell consisting of six nanosheets leads to an acceptable fit, as evidenced by an $R_{\rm W}$ of 0.23 over a wide range (2–60 Å). We did not include any chlorides or oxides of silicon in our model. Presumably the $R_{\rm W}$ could be further decreased by including these species, but their sparsity would require prohibitively large unit cells to capture the appropriate composition. Further, there have been a number of reported structures for SiNSs in the literature, called "siloxenes". So, we calculated the PDF of these siloxenes (Figure S2). One such structure consists of $\mathrm{Si}_6\mathrm{H}_6$ rings connected *via* SiOSi bridges, while the other consists of 1D (SiH)_n chains connected *via* SiOSi bridges (Figures S2, S9, and S10). These structures do not fit the data, with $R_{\rm W}$ values of 1.72 and 1.64, respectively.

Close inspection of the AI-spXRD reveals low-intensity features with narrow line widths. These features correspond to TaSi₂, a common contaminant that emerges from the synthesis of CaSi₂ in Ta tubes (see Methods for experimental details).²⁷ We would like to point out that these TaSi, features were not detected in the CaSi2 precursor using a laboratory diffractometer (Figure S1). Further, we conclude that the TaSi2 is likely in very low abundance given that crystalline materials are expected to exhibit much stronger diffraction intensities compared to the disordered SiNSs, ceteris paribus. Thus, the structure of our SiNS sample is best described by a hexagonal arrangement of buckled Si(111) monolayers, where each Si atom is chemically bonded to three other Si atoms and one H, and the stacking sequence of these sheets is similar to the initial stacking sequence in the CaSi2 precursor, but with a large degree of disorder in the intersheet spacing. The origin of the intersheet spacing disorder is unclear and should be a subject of future research, but we speculate that it may be a result of the inhomogeneous formation of H₂ bubbles²⁸ between sheets during deintercalation. In addition, the disorder in the intersheet spacing could emerge from the anisotropic formation and diffusion of relatively large $Ca^{2+}(H_2O)_x$ complexes during deintercalation.

Light-emitting SiNSs could be used in optoelectronic devices. An important aspect when considering implementing materials into practical devices is their thermal stability. Considering that many electronic and optoelectronic devices must remain operable at temperatures as high as 125 °C, we investigated the structural and optical properties of the SiNSs at elevated temperatures. To our surprise, we find that the SiNSs are stable at temperatures far exceeding this metric.

The above discussion was restricted to unannealed SiNSs; in the remaining portion of the article, we will discuss annealed SiNSs. The SiNSs were annealed at different temperatures in a glovebox filled with nitrogen (N₂), cooled to room temperature, and sealed in polyimide capillaries under an argon atmosphere. Total X-ray scattering was measured at Argonne National Laboratory Advanced Photon Source (APS), beamline 11-ID-B (see Methods). The PDF and AI-spXRD of the annealed SiNSs are shown in Figure 5. The PDF and AI-spXRD change very little up to 300 °C, but a broadening of all the peaks in the AI-spXRD begins between 300 and 350 °C (Figure 5b and Figure S6). This broadening continues to increase to 425 °C, whereupon the resulting AI-spXRD resembles that of amorphous Si (a-Si). In this temperature

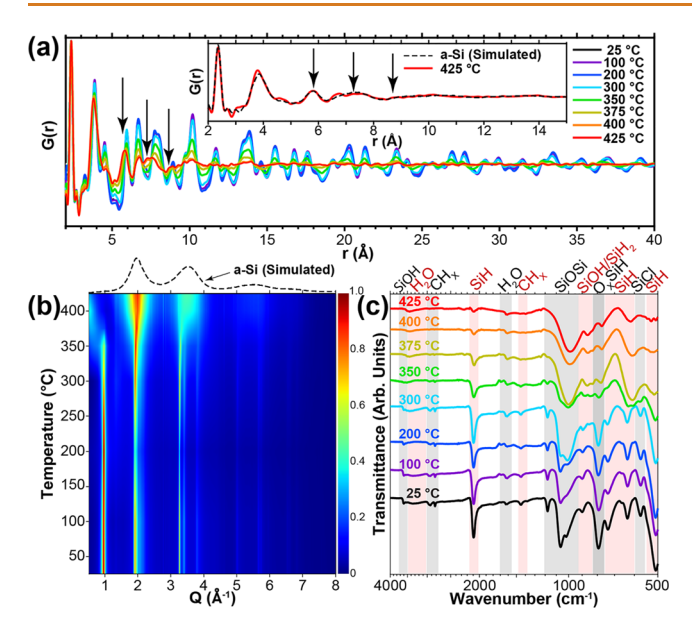


Figure 5. Structural and chemical properties of annealed SiNSs. All data were collected at room temperature. (a) PDF of SiNSs annealed at different temperatures. Inset is the PDF of the sample annealed at 425 °C and a simulation of the PDF of a-Si (see Methods). (b) AI-spXRD mapped over annealing temperatures. Above the figure (black dashed line) is a simulation of pXRD of a-Si. (c) FTIR of annealed SiNSs; note that the x-axis is on a logarithmic scale. Vertical red and gray bands are to guide the eye. The assignments on the top of the figure correspond to the unannealed sample (25 °C). See Table S1 for peak assignments for every temperature.

range, all PDF peaks that correspond to the 2D SiNSs begin to decrease their intensity, while the systematic absences in the SiNSs that occur in 3D bulk c-Si begin to increase their intensity (black arrows in Figure 5a). At 425 °C, peaks exist in the PDF at 5.8, 7.3, and 8.7 Å corresponding to the peaks of a-Si at 5.46, 7.06, and 8.65 Å, respectively. This indicates that the 2D framework begins to form additional bonds along the caxis. However, the slight deviation in the peak locations after annealing at 425 °C indicates that the transformation into a-Si is not complete, and additional Si-Si bonds would continue to form at temperatures of >425 °C; this hypothesis is later probed with UV-vis (vide infra). Further, upon inspecting the PDF and AI-spXRD at 425 °C, the resemblance to a-Si becomes apparent. Indeed, the PDF and AI-spXRD both suggest that the 2D SiNSs undergo structural amorphization to a-Si beginning at temperatures near 300 °C; this is done so by forming Si-Si bonds in the third dimension.

We previously used a combination of Raman, FTIR, and density functional theory (DFT) to assign every discernible peak within the FTIR spectrum of H-terminated SiNSs between 500 and 4000 cm⁻¹. With this knowledge, the chemical bonding of the annealed SiNSs was investigated with FTIR (Figure 5c). At temperatures below 200 °C, the only prominent change in the IR spectra is the loss of water between 100 and 200 °C and is consistent with our previous findings. Though it is clear that every FTIR spectrum exhibits water vibrations at ~1600 and ~3400 cm⁻¹ and it is likely that water molecules are intercalated at temperatures below 100 °C, we find it unlikely that water would persist in the sheets at much higher temperatures; thus, we attribute these vibrational modes at temperatures above 200 °C to

adsorbed or intercalated atmospheric water, as these data were collected under ambient conditions. We acknowledge that these features could arise from SiOH modes; however, our previous 12 and current (Figures S14 and S21) DFT calculations do not indicate any FTIR-active SiOH vibrations in SiNSs at $\sim\!1600~{\rm cm}^{-1}.$

Using DFT, we calculated the geometrically optimized structures, FTIR-active vibrational modes, and band structures of 11 distinct oxygen-containing structures of SiNSs to probe the properties and energetics associated with the insertion or rearrangement of oxygen within the SiNSs that may occur upon thermal annealing. In the respective unit cells, four structures contain a single oxygen (Figures S11-S14), three structures contain two oxygens (Figures S15-S17), three structures contain three oxygens (Figures S18-S20), and one structure contains four oxygens (Figure S21). Importantly, the calculations of the FTIR modes presented here (see Supporting Information for additional details) indicate that we may have previously incorrectly assigned the FTIR feature at ~793 cm⁻¹ to be SiO; 12 these present calculations indicate that this feature corresponds to the SiH wagging of O_xSiH (see GIFs in the Supporting Information for vibration visualization). In addition, we identified a previously unassigned feature in the experimentally measured FTIR: we find that the shoulder on the low-wavenumber side of the SiH feature centered at \sim 2100 cm $^{-1}$ can arise from SiH groups bonded to one or more oxygen atoms (O_xSiH). We find no additional inconsistencies with our previously assigned FTIR features.

We also used DFT to assess the thermodynamics of oxygencontaining defects. By comparing the enthalpies of different oxygen-containing configurations, we find that it is enthalpically favorable for an oxygen atom to insert itself within a Si-Si bond in SiNSs to form Si-O-Si, and this Si-O-Si configuration is more energetically favorable than SiOH (see Figure S22 for additional details). Further, our results indicate that it is enthalpically favorable for an oxygen to insert itself into the Si-Si bond if one of the Si atoms already contains at least one Si-O bond (see Figure S22 for additional details). In other words, after the first oxygen is inserted into a Si-Si bond (e.g., Figure S12), our calculations indicate that it is enthalpically favorable for a subsequent oxygen atom to attack the Si atom that already has an Si-O bond to yield an SiO₂ specie (e.g., Figure S15); we also find that it is enthalpically favorable to form SiO₃ after SiO₂ has been formed (e.g., Figure \$18). Interestingly, we find that after three oxygen atoms have surrounded a given Si atom (i.e., O₃SiH), we find that it is not enthalpically favorable to form O₃SiOH. Lastly, we find that the three-oxygen-containing structures are more enthalpically favorable than the siloxene structures (Figures S9, S10, and S22).

Comparing the FTIR spectra of SiNSs annealed at 200 and 300 °C, the largest change occurs between ca. 950 and 1200 cm⁻¹, the SiOSi region. As the temperature increases, there is an increase in the intensity of the SiOSi feature centered at ~1015 cm⁻¹. Despite the increase in intensity of the SiOSi feature, the O_x SiH mode at 793 cm⁻¹ does not increase its intensity, further corroborating the DFT prediction that oxygen atoms preferentially attack Si–Si bonds where one of the Si atoms already has an Si–O bond and that the feature at 792 cm⁻¹ is associated with the SiH wagging of O_x SiH rather than SiO. We hypothesize that this change in the SiOSi region results from chemical reactions with residual intercalated water or trace amounts of O_2 that were in the N_2 -filled glovebox

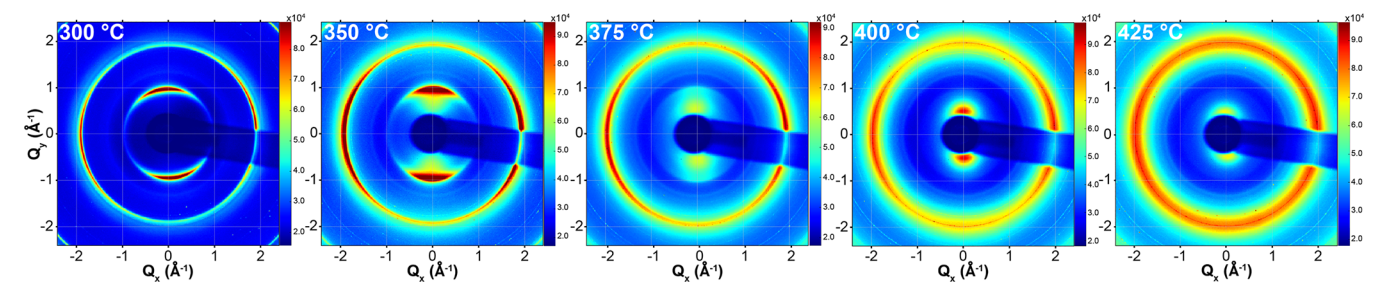


Figure 6. 2D-spXRD of annealed SiNSs, with the annealing temperature indicated on the top left of each diffractogram. All data were collected at room temperature. See Figure S7 for the full-scale 2D-spXRD diffractograms for all temperatures.

while annealing the samples, or the insertion or rearrangement of the oxygen of SiOH into Si-Si bonds. Furthermore, X-ray photoelectron spectroscopy (vide infra) indicates that there is a slight increase in the concentration of the Si²⁺ and Si⁴⁺ oxidation states in this temperature range (Figure 7), consistent with the formation of SiO2, or SiO4. At increased annealing temperatures, the FTIR-active SiOSi mode continues to broaden and shift toward lower wavenumber, suggesting a structural relaxation and the formation of disordered SiOSi species. Despite the relatively large SiOSi FTIR features, it is important to note that the intensity of each FTIR peak does not indicate the relative concentration of those species, with the absorption cross-section of the SiOSi mode at $\sim 1000 \text{ cm}^{-1}$ being ~ 30 times greater than that of the SiH mode at ~2100 cm⁻¹ for the same concentration of SiOSi and SiH.12

At annealing temperatures between 300 and 350 $^{\circ}$ C, a substantial decrease in the FTIR peak intensity at 570 cm⁻¹ is observed, corresponding to the loss of Cl from Si₃SiCl. This is consistent with our previous finding that HCl is liberated at temperatures above ~350 $^{\circ}$ C. ¹² In addition, between 300 and 350 $^{\circ}$ C, the SiH modes at ~500, ~633, ~737, and ~2100 cm⁻¹ and the O_xSiH mode at 793 cm⁻¹ all begin to decrease in intensity; we attribute this to a loss of H and Cl in the form of H₂ and HCl. The fact that the well-known SiH feature at ~2100 cm⁻¹ decreases in intensity in tandem with the decrease in intensity of the feature at 793 cm⁻¹ further supports our assignment of this feature as O_xSiH. Moreover, in this temperature range, the SiOSi mode at ~1000 cm⁻¹ continues to shift to lower energies, and the SiOSi features at 1065 and 1080 cm⁻¹ have nearly completely merged.

The largest differential change in the FTIR occurs between 350 and 375 °C. All of the peaks between ca. 570-630 cm⁻¹ combine into a single broad feature centered at $\sim 602 \text{ cm}^{-1}$ by 375 °C; we suspect that the features between ca. 570 and 630 cm⁻¹ are related to SiH-, SiO-, and/or SiOH-containing species. The O_xSiH feature at ~793 cm⁻¹ becomes less intense and begins to shift toward lower wavenumber; however, a substantial overlap with other peaks in this region in conjunction with the loss in SiH at these temperatures makes precise interpretation difficult. The feature corresponding to SiO and SiH₂ at ~900 cm⁻¹ completely disappears, while two new peaks emerge at 829 and 833 cm⁻¹, likely as a result of the loss of H and structural relaxation of silicon oxides. This stark shift in the peak at ~900 cm⁻¹ to a lower energy is consistent with the lowering in energy of other SiO modes at this temperature. Finally, the SiOSi peak at 1065 cm⁻¹ is no longer visible.

Between 375 and 425 °C, the FTIR spectra change very little, except for the emergence of small unidentified features at

wavenumbers just greater than 500 cm $^{-1}$. At 425 °C, the dominant features are SiO and SiH. The peak at \sim 1178 cm $^{-1}$ is no longer detected. At 425 °C all of the SiH modes are still present—albeit severely suppressed—suggesting that SiH is present within the a-Si network, which is typical of a-Si thin films.

A previous study of germanane—the germanium analogue to silicane—demonstrated that germanane begins to amorphize at 75 °C, accompanied by a contraction of the intersheet spacing at 150 °C. Surprisingly, we find that the Si framework is structurally stable at temperatures less than ~ 300 °C. At temperatures greater than 300 °C, the AI-spXRD (Figure 5b) indicates that the peak corresponding to the intersheet spacing (at Q < 1 Å⁻¹) begins to broaden and shift to lower Q, indicating an *expansion* of the intersheet spacing. We attribute this expansion to the coalescence of adjacent 2D sheets as intersheet Si—Si bonds form, and we justify this hypothesis in the following four paragraphs.

Upon inspecting the 2D-spXRD data, there is a clear resemblance in the diffractograms for the unannealed sample (Figure 4) and the sample annealed at 300 °C (Figure 6), indicating that the structure of the SiNSs is stable at temperatures less than ~300 °C. At annealing temperatures of 350 °C (Figure 6), there is a clear shift in the peak corresponding to the intersheet spacing (at Q < ${\sim}1~\mbox{\normalfont\AA}^{-1})$ to larger d-spacing while retaining its orientation along $Q_X = 0$ Å-I (the vertical axis), while the peak that corresponds to intersheet registry $(Q_{(100)} \approx 2 \text{ Å}^{-1})$ retains its orientation along $Q_{\rm Y} = 0 \text{ Å}^{-1}$ (the horizontal axis). This suggests that the annealed SiNSs initially begin to coalesce with each other while keeping their translational alignment. However, between 400 and 425 °C, the preferred orientation of the peaks corresponding to the (hk0) planes along $Q_Y = 0 \text{ Å}^{-1}$ is lost, suggesting that the translational order among adjacent SiNSs is lost, likely due to the amorphization of the SiNSs. We find that this intersheet spacing approximately doubles from a *d*-spacing of 6.48 Å (Q = 0.97 Å⁻¹) for the unannealed sample (Figure 4) to 11.9 Å (Q = 0.53 Å⁻¹) by 400 °C; this is consistent with the formation of amorphous nanosheets, whereby, on average, two adjacent nanosheets coalesce. Additionally, we do not detect Bragg diffraction from the newly formed multilayer sheets, likely as a result of the amorphicity of the Si framework. Importantly, we do not anticipate that the coalescence is uniform across sheets.

Scanning electron microscopy (SEM) images (Figure S8) indicate annealed SiNSs do not exhibit morphological changes in the sheet-like structure or translational alignment and do not indicate an overall volume expansion, further supporting that the coalescence is occurring on short length scales. The coalescence is supported by the PDF data as well (Figure 5a),

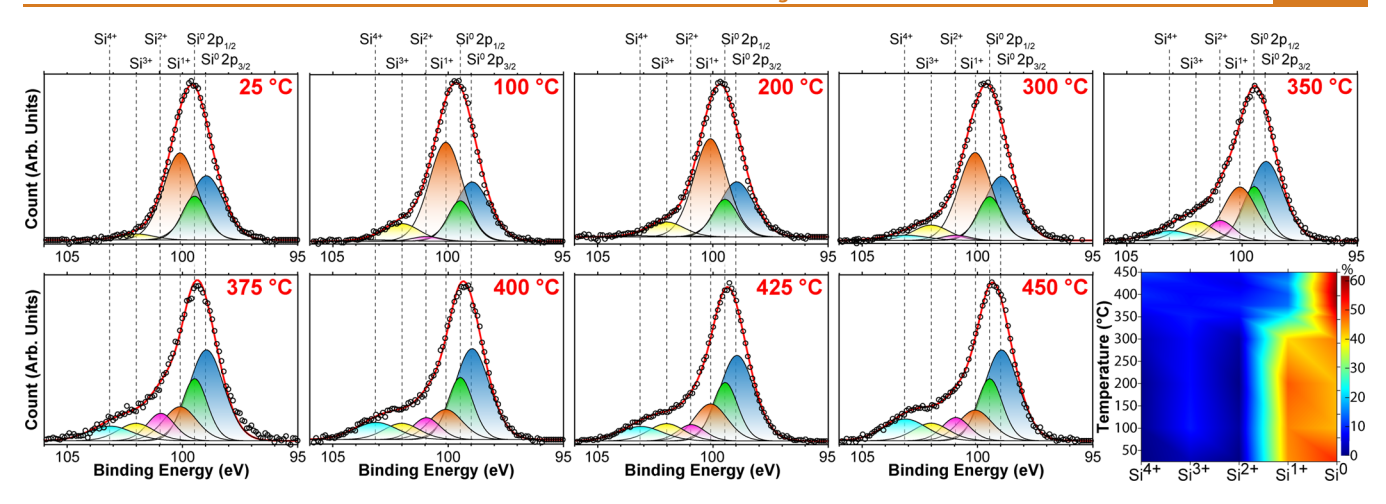


Figure 7. XPS with peak deconvolution of annealed SiNSs. All data were collected at room temperature. Experimental data are plotted in black circles, and the sum of each fit is shown as a red line. Vertical dashed lines indicate the binding energies of $Si^0 2p_{3/2}$, $Si^0 2p_{1/2}$, Si^{1+} , Si^{2+} , Si^{3+} , and Si^{4+} centered at 99.0, 99.5, 100.1, 100.9, 102.0, and 103.1 eV, respectively. The red number in the top right of each spectrum indicates the temperature at which the sample was annealed, with 25 °C corresponding to the unannealed sample. The panel on the bottom right is a heatmap of the percent contribution of each oxidation state as determined by the peak fits.

where the 3D Si–Si bonds begin to form at elevated temperatures ($vide\ supra$), and by at 425 °C, the disappearance of the PDF features at radial distances greater than ~15 Å implies a loss of long-range order, which likely arises from the amorphization of the Si framework with pair—pair correlations extending only to ~15 Å. Another possibility that could explain the increase in the intersheet spacing is that the expansion of evolved gas (H_2 and HCl) pushes the sheets apart, but again SEM does not indicate any macroscopic expansion of the sheets, and the formation of 3D Si–Si bonds negates this notion.

The coalescence of annealed SiNSs is also supported by the evolution of HCl gas 12 and the decrease in the FTIR SiH feature as the SiNSs are heated to 350 °C; indeed, we find a large increase in the number of dangling bonds at temperatures greater than 300 °C (*vide infra*). If we consider two adjacent nanosheets, labeled as "1" and "2", we conjecture that a surface radical associated with a Si atom on sheet 1 (named " $^{\bullet}$ Si 1 ") reacts with another surface radical associated with a Si atom on sheet 2 (named " $^{\bullet}$ Si 2 "), as described by the following: $^{\bullet}$ Si 1 + $^{\bullet}$ Si 2 \rightarrow Si 1 -Si 2 . Once an initial bond is formed, the force defined by the bond in the Si 1 -Si 2 moiety keeps the sheets together such that continued propagation of intersheet bond formation can proceed.

Overall, these combined data indicate that at temperatures greater than 300 $^{\circ}$ C the increased distance of X-ray scattering centers associated with the X-ray scattering peak at Q < 1 Å is a result of SiNS coalescence, which arises from the formation of dangling bonds during amorphization as H and Cl are liberated from the SiNSs. This coalescence progresses such that the overall distance between scattering centers (coalesced stacks of sheets) increases, where on average, two sheets combine, resulting in a minimal overall volume change.

We collected X-ray photoelectron spectroscopy (XPS) data of the annealed SiNSs (Figure 7). To deconvolve the XPS spectra, the binding energies and the full width at half-maximum (fwhm) of each oxidation state were kept constant across all spectra, but were chosen by simultaneously minimizing the sum of squared residuals for *all* spectra. Further, the area of the Si 0 2p $_{3/2}$ peak was precisely twice that of the area of the Si 0 2p $_{1/2}$ peak. Only the relative intensities of

each oxidation state were allowed to differ from sample to sample (see Methods for additional details). Comparing the spectra associated with annealing temperatures of 300 and 350 °C, the relative contributions of Si⁰ and Si¹⁺ shift; at 300 °C, the spectrum is comprised of $\sim 45\%$ Si⁰ and $\sim 40\%$ Si¹⁺, while at 350 °C it is comprised of ~55% Si⁰ and ~25% Si¹⁺. This increase of the Si⁰ and decrease of the Si¹⁺ contribution continues until ~400 °C, after which the change in contributions plateaus with respect to temperature. This change in oxidation state is consistent with our proposed mechanism, where additional Si-Si bonds form as H is liberated from the SiNSs, thereby decreasing the Si¹⁺ concentration and increasing the Si⁰ concentration. Comparing the spectra associated with annealing temperatures of 300 and 450 °C, there is an increase in the concentration of the Si⁴⁺ oxidation state, while the concentration of the Si²⁺ and Si³⁺ oxidation states stay relatively constant. The final product at 450 °C is composed of $\sim 60\%$ Si⁰ and $\sim 10\%$ each of Si¹⁺, Si²⁺, Si³⁺, and Si⁴⁺.

Summarizing the structure and surface chemistry of SiNSs annealed at different temperatures, we find that upon heating the SiNSs for 10 min between room temperature and 300 °C, the PDF and AI-spXRD indicate little to no structural changes in the Si framework, while FTIR demonstrates that water is liberated between 100 and 200 °C. Between 200 and 300 °C, FTIR indicates a change in the SiOSi features, likely arising from structural rearrangement of silicon oxides or chemical reactions with O2 or water. However, XPS gives little indication of what types of silicon oxides may form between 200 and 300 °C, with only a slight decrease of the Si¹⁺ and an increase in the Si⁰, Si³⁺, and Si⁴⁺ species. The wide range of oxidation states associated with this subtle change in the FTIRactive SiOSi feature at \sim 1015 cm⁻¹ indicates that this feature is not composed of a single component. Between 300 and 350 °C, FTIR indicates that hydrogen is liberated, while XPS shows a sudden increase (decrease) of the Si⁰ (Si¹⁺) features corresponding to SiSi (SiH), and all of the AI-spXRD peaks begin to broaden and the (006) peak begins to shift to larger dspacing; these data can be interpreted as the loss of the terminal hydrogen and subsequent formation of intersheet Si-Si bonds to yield coalesced amorphous SiNSs. The

amorphization and coalescence continues through 425 °C, where there is little change in the SiO species in FTIR, and the peak corresponding to the initial (006) plane in AI-spXRD continues to shift to larger *d*-spacing in tandem with a broadening of all AI-spXRD peaks. Between 350 and 425 °C, a shortening of the maximum pair—pair correlation distance is apparent in the PDF data, and PDF scattering pairs that correspond to 3D Si—Si bonds begin to appear. SEM indicates no morphological changes during the entire temperature range. All of these data combined suggest that the SiNSs begin to lose their terminal hydrogens and form amorphous Si—Si bonds with adjacent nanosheets to yield amorphous SiNSs beginning at ~300 °C.

To investigate the effects of annealing duration on the FTIR spectra, we annealed SiNSs for 48 h at 100, 125, 150, 200, 250, and 300 °C under an atmosphere of N₂ (Figure S26a). FTIR indicates a miniscule observable change up to and including 150 °C except for a slight decrease in the water vibrations at \sim 3400 and 1600 cm⁻¹, which we attribute to the liberation of intercalated water. At 200 °C, we observe a very slight increase in intensity of the SiOSi mode at ~1015 cm⁻¹; this shift is not accompanied by a dramatic decrease in the SiOH modes, and as such, we do not expect that this is related to the structural rearrangements of SiOH. We do, however, suspect that this shift is related to reactions involving the Si framework and oxygen-containing molecules. Residual intercalated water is expected to react with the SiNSs at these elevated temperatures; however, given that the annealing environment had detected O2 concentrations of ~0.1-1 ppm, we cannot exclude reactions with trace environmental O_2 over the course of the 48 h annealing duration. At 250 °C, there is a stark increase in SiOSi and a decrease in SiOH; this suggests that SiOH features begin to rearrange such that the oxygen of the SiOH is inserted between Si-Si bonds to yield SiOSi species. After 48 h at 300 °C, the SiOH modes are nearly indiscernible, and the SiOSi mode has further increased, indicating additional insertion of oxygen into the Si framework. Further, at 300 °C, the SiH feature has decreased in intensity by approximately half, indicating the liberation of H from the surface. We find that the FTIR spectrum of SiNSs annealed at 300 $^{\circ}\text{C}$ for 48 h most closely resembles that of SiNSs that were annealed at 375 °C for 10 min.

We investigated the diffuse reflectance absorbance, steadystate photoluminescence (PL), and time-resolved photoluminescence (TRPL) of the annealed SiNSs (Figure 8). Upon annealing the SiNSs, we observe a color change beginning at ~350 °C; the color of the nanosheets changes from yellow-green, to yellow, orange, red, and finally to black. This color change is similar to what Harris and co-workers observed in a-Si nanoparticles.³³ They reported on a-Si nanoparticles that were synthesized at temperatures between 380 and 550 °C, whose colors ranged from yellow to deep red to dark purple over this temperature range. They attributed these color differences to the hydrogen content and structural order. Given our analysis of the FTIR and XRD above, our results support the assertion that differences in color are related to the hydrogen content within the SiNSs and structural order. However, we find that our nanosheets exhibit a color change at temperatures slightly below their nanoparticles.³³ Further, in their work, they found that at temperatures greater than ~450 °C the particles began "necking" and some sintering of neighboring particles occurred. Similarly, our XRD suggests a similar coalescence

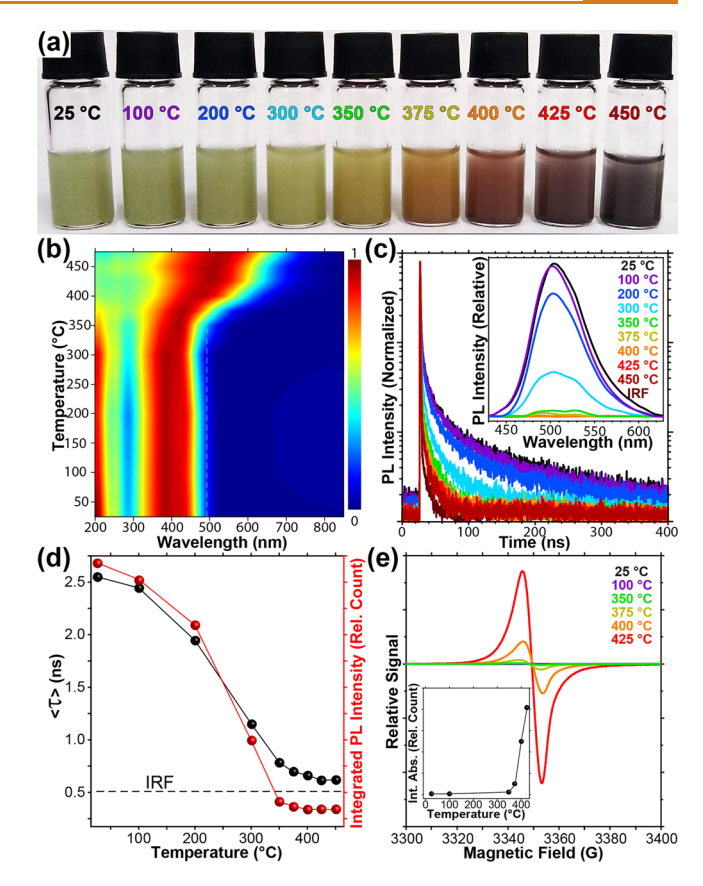


Figure 8. Optical properties of annealed SiNSs. All data were collected at room temperature. (a) Photograph of the annealed samples dispersed in methanol at 3 mg/mL. (b) Heat map of the Kubelka–Munk transformation of diffuse reflectance spectra; vertical dashed line at 495 nm is to guide the eye. (c) Timeresolved photoluminescence of annealed SiNSs at a concentration of 0.5 mg/mL; inset is the corresponding steady-state photoluminescence. (d) Average photoluminescence lifetime (left, black axis) and total integrated photoluminescence intensity (right, red axis). Horizontal dashed line corresponds to the IRF lifetime. See Table S2 for peak fitting parameters. (e) Electron paramagnetic resonance of annealed SiNSs; inset is the relative integrated EPR absorbance signal.

behavior begins to occur at \sim 350 °C. We attribute the temperature differences in these systems to be a result of the dimensionality, with the nanosheets exhibiting a much higher concentration of Si–H bonds.

To quantify the visible changes in color that occurred upon annealing the SiNSs, we collected diffuse reflectance data and used the Kubelka-Munk (KM) function to transform these data into pseudoabsorbance (Figure 8b). Similar to the FTIR data above, we observe no appreciable difference in the KM line shape up to 200 °C. However, at 300 °C, there is a blueshift in the onset of absorption from its value of ~501 nm (2.48 eV) at 25 °C to \sim 486 nm (2.55 eV) at 300 °C, but this blue-shift is then reversed back to its initial onset of absorption by 350 °C. We would like to point out that this blue-shift is reproducible and has been reported before in the literature in studies of "siloxene". 34 This blue-shift could be due to chemical reactions with water or trace O₂ within the N₂-filled glovebox or the insertion or rearrangement of the oxygen of SiOH into Si-Si bonds. Given that the DFT results presented above indicate that the formation of SiOSi is more favorable than the formation of SiOH, we suspect that such reaction with water or O_2 would yield O_x –Si–Si $_{3-x}$ bonds. At temperatures greater than 350 °C, we find that the onset of absorption begins to shift toward the red. We attribute this red-shift to the structural disorder and consequently a distribution of allowed optical transitions with energies less than that of the unannealed SiNSs. By 475 °C, the onset of absorption occurs near 1.65 eV, consistent with a-Si.

To further investigate the effects of annealing duration, we determined the KM function of SiNSs that were annealed for 48 h at 100, 125, 150, 200, 250, and 300 °C (Figure S26b) under a N2 atmosphere with a concentration of detected O2 of ca. 0.1-1 ppm. It is clear that there are few changes to the absorption of SiNSs annealed at temperatures up to and including 250 °C (Figure S26b). However, upon annealing at 300 °C for 48 h, we observe that the onset of absorption shifts toward the red and all of the absorbance features broaden, which is consistent with amorphization. We find that the KM function associated with SiNSs annealed at 300 °C for 48 h most closely resembles that of SiNSs that were annealed at 375 °C for 10 min, consistent with FTIR of SiNSs annealed for 48 h (vide supra). Interestingly, we note that the SiNSs do not turn black after 48 h of heating at 300 °C, unlike SiNSs that were annealed at ~450 °C for 10 min (Figure 8a); this indicates that the entire amorphization process is not a single step, but instead involves discrete reaction steps, each with their own associated activation energy.

We would like to briefly point out that many Si nanomaterials exhibit a peak in the absorbance spectrum near 270–340 nm that is attributed to the $\Gamma \to \Gamma$ transition within the band structure. ^35,36 In contrast, we observe a valley in the absorbance for SiNSs in this same energy range (Figure 8b). This demonstrates a clear difference in the electronic excited states of SiNSs and other low-dimensional forms of Si. Additionally, at annealing temperatures between 300 and 350 °C, this valley in the absorbance at ~280 nm is suppressed, leading to a relative increase in absorbance near 280 nm at all temperatures above 350 °C.

Comparing the light-emitting properties for samples annealed at 200 and 300 °C, there is a large decrease in both the PL intensity and lifetime by 300 °C. In this temperature range, we also observe an increased intensity in the SiOSi region in FTIR (infra supra), a blue-shift in the onset of absorption, and a slight emergence of Si²⁺ and Si⁴⁺ in XPS, suggesting the formation of silicon oxides. Thus, we attribute the decrease in PL intensity, decrease in lifetime, and blue-shift in the onset of absorption at 300 °C to the formation of glass-like silicon oxides. At temperatures above 300 °C, we observe a monotonic decrease in the PL intensity and lifetime until 475 °C, where emission is nearly undetected. We find that the trend of the integrated PL intensity with respect to temperature resembles that of the relative photoluminescence quantum yield (PLQY) of SiNSs (Figure S27), with a PLQY maximum associated with the unannealed samples and a monotonic decrease with increasing annealing temperatures. Importantly, the inability to prepare nonscattering solutions of SiNSs prevents accurate measurements of the absorbance and photoluminescence emission intensity, as scattering samples introduce many complications when determining the PLQY.³⁷ As such, the solubilization of SiNSs should be a subject of future research.

Electron paramagnetic resonance (EPR) data (Figure 8e) indicate an increase in Si dangling bonds (g = 2.0103) at temperatures $\geq \sim 300$ °C; these dangling bonds are known to

result in nonradiative defects. $^{38-40}$ The increase of Si dangling bonds at $\sim 300\,^{\circ}$ C is consistent with a prior report. Further, our DFT calculations support that Si dangling bonds form midgap states (Figure S23). As such, we attribute this continued decrease in lifetime and PL intensity to the formation of dangling bonds.

We fit the PL spectra to two Gaussian distributions centered at \sim 2.5 and \sim 2.35 eV. We find that the total integrated area of the high-energy feature decreases monotonically. The total integrated area of the low-energy feature increases with annealing temperatures between 25 and 200 °C and decreases at higher temperatures. Interestingly, we note that the PL peak position is independent of annealing temperature, suggesting that the dominant recombination pathways remain mostly unchanged throughout the thermal degradation process.

Summarizing the optical properties of SiNSs thermally annealed for 10 min, between 25 and 100 °C, we observe a small decrease in PL intensity and lifetime and no changes in the optical absorbance. Between 100 and 200 °C, there is a decrease in the PL intensity and excitonic lifetime that may arise from the formation of dangling bonds that form upon the homolytic cleavage of SiH bonds or could result from a loss of water. Annealing in the range of 200 and 300 °C is accompanied by the largest relative decrease in PL intensity and lifetime, which we attribute to the formation of additional dangling bonds. At ~300 °C, a blue-shift in the absorption onset occurs, which we attribute to the formation of SiOx species; the dip in absorbance at ~280 nm is suppressed in this temperature range, likely emerging from structural distortions as the hexagonal Si framework undergoes amorphization. In the range of 350 to 475 °C, there is a monotonic red-shift in the onset of absorption, a monotonic decrease in both the PL intensity and excitonic lifetime, and a monotonic increase in the concentration of dangling bonds as the annealing temperature increases.

CONCLUSION

In conclusion, we report on the long-range structural properties, anisotropic disorder, vibrational properties, optical properties, and the thermal decomposition of silicane. We used total X-ray scattering, atomic pair distribution function analysis, structure refinement, SEM, FTIR, XPS, UV-vis, steady-state and time-resolved photoluminescence, and EPR to characterize the decomposition and DFT calculations to support our conclusions. We confirm that the SiNSs consist of an atomically thin silicon backbone arranged in a buckledhoneycomb pattern that is predominantly terminated with hydrogen. Our structural analysis also suggests that the SiNSs exhibit anisotropic disorder, having disorder within the intersheet spacing, but have little translational or rotational disorder among adjacent SiNSs. On average, the SiNSs retain the same stacking sequence as the CaSi2 precursor. We investigated the thermal decomposition of the SiNSs by heating under an inert atmosphere. We find that the SiNSs begin to lose their terminal hydrogens and form amorphous Si-Si bonds with adjacent nanosheets to yield coalesced amorphous silicon nanosheets beginning at ~300 °C and continue to amorphize through 450 °C without significant changes to the sheet-like morphology. This indicates that the Si framework of the SiNSs is resistant to thermal degradation, even when annealed for 48 h. In addition, we investigated the thermal stability of optical properties of the SiNSs. We find that PL intensity decreases upon annealing to temperatures

greater than 200 °C, which is likely a result of the formation of Si dangling bonds *via* hemolytic cleavage of Si–H bonds or the loss of intercalated water; this is supported by an increase in EPR signal and a decrease in the SiH signal in FTIR. The PL is nearly completely absent upon annealing at temperatures exceeding ~375 °C, which coincides with the liberation of terminal hydrogen atoms and a rapid increase in the quantity of dangling bonds as detected by EPR. The thermal degradation process demonstrates the need to identify functionalization strategies that result in high surface coverage with thermally robust surface chemistry. The results presented in this work demonstrate that SiNSs can be considered as a viable CMOS-compatible optoelectronic material and that the SiNSs are stable at the most stringent of operating temperatures.

MATERIALS AND METHODS

CaSi₂ Synthesis. CaSi₂ was synthesized by placing silicon and calcium into a tantalum tube, with slight stoichiometric excess silicon to prevent the formation of undesired phases and to replenish any consumed Si that reacts with the tantalum tube. All work for the synthesis of CaSi2 was performed in a glovebox filled with argon. CaSi₂ was synthesized by placing 2.991 g of Si pieces (Sigma-Aldrich 99.95%) and 1.967 of Ca granules (Sigma-Aldrich 99%) into a Ta tube (molar ratio of Ca:Si is 1:2.125) The tube was crimped shut and subsequently welded shut with a GTAW welder (Miller Maxstar 210). Warning! The Ta tube must be long enough to avoid overpressurization of the tube! Overpressurization can cause tube failure and a sudden release of molten material! This reaction should be performed in an inert atmosphere, such as a glovebox! The tube containing the Ca and Si was placed into the coil of an induction heater, and the contents were melted and mixed thoroughly. Then, while the contents were melted, the tube was quickly cooled by placing the red-hot tube into a container filled with aluminum chips to avoid peritectic decomposition. The sealed tube was then removed from the glovebox, and the exterior of the tube was cleaned with concentrated hydrochloric acid to remove any aluminum that adhered to the tube. Finally, the tube was rinsed with DI water, dried, moved back into an argon-filled glovebox, and opened to yield chunks of CaSi₂.

SiNS Synthesis. In a glovebox filled with N_2 , the $CaSi_2$ synthesized above was ground to a fine powder using a mortar and pestle. Then, 3.05 g of this powder was placed in a vial and chilled to -35 °C. In a separate, 500 mL round-bottom three-necked flask, 310 mL of concentrated HCl was added, placed in the freezer set at -35 °C, and connected to a Schlenk line under flowing forming gas (5 mol % H_2 , 95 mol % N_2). The flask was purged for a few minutes with forming gas to rid the head space of oxygen. The flask was allowed to chill to -35 °C overnight. The next day, the $CaSi_2$ was added to the flask under a continuous flow of forming gas. The reaction contents were allowed to sit unstirred at -35 °C for 11 days. After 11 days, the contents were filtered under an inert atmosphere and washed with \sim 250 mL of anhydrous methanol (ACS grade), followed by a final wash with \sim 50 mL of anhydrous acetonitrile. Finally, the product was dried under vacuum for \sim 80 h.

Sample Annealing. All annealing procedures were performed in a glovebox filled with N_2 . To anneal the samples, ~ 50 mg of the asprepared SiNSs was placed into an 8 mL glass vial. Then, a hot plate equipped with an aluminum reaction block—containing holes sized to fit the vials—was heated to the desired temperature. The temperature was measured in the aluminum block with an external thermometer. Once the desired temperature was reached in the reaction block, the vial containing the SiNSs was then placed in the aluminum block for 5 min, then briefly shaken to mix the SiNSs, and finally allowed to anneal for an additional 5 min. After 10 min of annealing, the SiNSs were removed from the aluminum block and allowed to cool naturally in the glovebox. All samples were stored under an inert atmosphere for characterization. For SiNSs annealed for 48 h, the above procedure was repeated, except the SiNSs were annealed for 48 h

and were shaken after 10 min and 24 h of annealing. All data in this article and associated Supporting Information correspond to samples annealed for 10 min unless otherwise specified.

Pair Distribution Function. Total scattering data were collected at the APS, Argonne National Laboratory, at the 11-ID-B beamline with a 2D detector at a distance of 180 mm and an X-ray energy of 58.63 keV (0.2115 Å); the axis of the capillary was perpendicular to the incident X-rays and parallel to the detector. The 2D total scattering data were azimuthally integrated with the GSAS-II software ¹² after calibrating to a CeO₂ standard to obtain synchrotron powder X-ray diffraction data (AI-spXRD). The PDFs were extracted with the PDFgetX2 software 43 by first subtracting an independently collected polyimide background. Structural refinement was performed with the PDFgui software; 44 protons were omitted during the refinement. Synchrotron powder X-ray diffraction data were collected at the APS, Argonne National Laboratory, at the 11-ID-B beamline. The detector distance was 1000 mm. Samples were packed into polyimide capillaries (Cole-Parmer, 0.0395 in. inner diameter, 0.0434 in. outer diameter) and sealed on both ends with two-part epoxy (Devcon, Stock #14270). The standard deviations of peak locations were calculated as follows:

$$\sigma = \frac{d_2 - d_1}{2\sqrt{2\ln(2)}}$$

where d_2 and d_1 correspond to the d-spacing associated with the upper and lower values of the fwhm, respectively.

Simulations of a-Si. The simulations of the PDF and pXRD of a-Si were performed with a unit cell described elsewhere. ⁴⁵ The unit cell contained 4096 atoms.

Powder X-ray Diffraction. XRD patterns of $CaSi_2$ were collected with a Bruker DaVinci D8 Advance diffractometer with a Cu K α radiation source.

Scanning Electron Microscopy. SEM images were collected with an FEI Teneo microscope. Samples were prepared by directly painting an aluminum SEM stub with carbon paint (Ted Pella, Inc.) or silver paint (Ted Pella, Inc.) and immediately depositing the sample onto the wet paint. The samples were dried and stored under N_2 until immediately before characterization.

Fourier Transform Infrared Spectroscopy. FTIR data were collected with a Nicolet iSS FTIR spectrometer with an iDS attenuated total reflectance (ATR) accessory. All data were collected under ambient conditions.

DFT. All DFT calculations were performed via plane wave DFT in VASP. 46,47 The exchange-correlation functionals were described by the PBE-GGA, 48 and the PAW 46,49,50 method approximated core electrons. All structures were relaxed until all forces and the selfconsistent-field energies were less than 0.01 eV/Å and 1×10^{-5} eV, respectively. The Brillouin zone was sampled with a k-point density of 8/Å-1 with an automatic Monkhorst-Pack grid. 51 The kinetic energy cutoff was 550 eV. Every structure, except for the refined PDF structure in the main text containing the six sheets per unit cell (Figure 1), contained at least 15 Å of vacuum spacing between adjacent sheets. FTIR spectra were simulated with techniques described elsewhere. S2-57 All FTIR peaks were fit to Lorentzian distributions with a fwhm of 50 cm⁻¹. All DFT-simulated FTIR spectra were calibrated as described in the following: to generate the calibration, we plotted our previously determined experimental wavenumber vs our previously determined corresponding DFT wavenumber (data are shown in the first two columns of Table S3 in ref 12) and fit a linear trend line, as shown in Figure S25.

X-ray Photoelectron Spectroscopy. XPS data were collected with a Kratos Amicus/ESCA 3400 instrument. The sample was irradiated with 240 W unmonochromated Al K α X-rays, and photoelectrons emitted at 0° from the surface normal were energy analyzed using a DuPont-type analyzer. The extrinsic loss structure was subtracted with a Shirley-type background. Data were calibrated to the C 1s peak to be 284.8 eV. For peak fitting, each oxidation state was fit to a Gaussian–Laurentz product function (GLP) with a mixing parameter that is 60% Gaussian. The binding energy and fwhm were

kept the same for every sample, but were optimized by minimizing the sum of squared residuals such that only the relative intensities of each distribution corresponding to an oxidation state were allowed to differ from sample to sample (see equation, below). Further, the area of the Si^0 $2\mathrm{p}_{3/2}$ was constrained to be precisely twice that of the Si^0 $2\mathrm{p}_{1/2}$ peak. We find an energy center (fwhm) of 99.0 (1.85), 99.5 (1.35), 100.1 (1.78), 100.9 (1.47), 102.0 (1.91), and 103.1 (2.31) eV for Si^0 $2\mathrm{p}_{3/2}$, Si^0 $2\mathrm{p}_{1/2}$, Si^{1+} , Si^{2+} , Si^{3+} , and Si^{4+} , respectively. XPS spectra were deconvolved and fitted to the data by evaluating the following equation, by changing the intensity of each distribution for each sample, the values of the center of each distribution corresponding to an oxidation state, and the fwhm of each distribution:

$$\min_{\underline{\mathbf{\Delta}}.\mathbf{C}.\mathbf{W}} \left[\sum_{\text{Sample},i=1}^{9} \left[\sum_{\mathbf{BE}_{i,j}=1}^{n} \left\{ Y_{\text{Model}_{i,j}} - Y_{\text{Obs}_{i,j}} \right\}^{2} \right] \right]$$

where
$$Y_{\text{Model}_{i,j}} - Y_{\text{Obs}_{i,j}} = \left(\sum_{\text{Dist},k=1}^{6} \mathbf{A}_{i,k} \text{GLP}(\mathbf{BE}_{i,j}; \mathbf{C}_k, \mathbf{W}_k)\right) - Y_{\text{Obs},i}(\mathbf{BE}_{i,i})$$

In the above equation, "i" is an index that runs over all nine samples. The samples correspond to the nine spectra in the temperature range of 25-450 °C shown in Figure 7. "j" is an index that runs over all binding energies for a given sample. "k" is an index that runs over all distributions. There are six distributions for each sample, corresponding to the Si⁰ 2p_{3/2}, Si⁰ 2p_{1/2}, Si¹⁺, Si²⁺, Si³⁺, and Si⁴⁺ oxidation states. "BE" is a $9 \times n$ matrix whose rows correspond to the sample number, and columns correspond to the binding energies shown in Figure 7. "C" is a 1 × 6 vector whose elements correspond to the center of each distribution. "W" is a 1×6 vector whose elements correspond to the fwhm of each distribution. "A" is a 9 × 6 matrix whose rows correspond to the sample number, and columns correspond to the amplitude of each distribution. "GLP" is the Gaussian-Laurentz product function with a mixing parameter that is 60% Gaussian. " $Y_{\text{Obs},i}$ " are the experimentally measured XPS intensities corresponding to sample "i". Note that the only fitting parameter that depends on the sample is $A_{i,k}$ as this was the only parameter that was allowed to differ for each i^{th} sample.

Diffuse Reflectance. To collect diffuse reflectance data, the sample was dispensed onto the adhesive side of clear packaging tape (3M Scotch packaging tape), and reflectance was collected of the bare SiNSs. The data were collected with a PerkinElmer Lambda 750 equipped with a Labsphere 100 mm integrating sphere, and the data were then subject to the Kubelka–Munk transformation.

Photoluminescence. PL data were collected with a PerkinElmer LS 55 with an excitation wavelength of 370 nm and slit widths of 5 nm. Suspensions were made at a concentration of 0.5 mg/mL in methanol.

Time-Resolved Photoluminescence. All TRPL data were collected with a Horiba DeltaFlex TCSPS and an excitation wavelength of 359 nm monitored at 510 nm. Suspensions were made at a concentration of 0.5 mg/mL in methanol. Data were fit to a triexponential: $I(t) = A e^{-t/\tau_1} + B e^{-t/\tau_2} + C e^{-t/\tau_3}$. The average lifetime was calculated with the amplitude average lifetime: $S^{S}(\tau)(A\tau_1 + B\tau_2 + C\tau_3)/(A + B + C)$. See Table S2 for fitting parameters. Qualitatively, the amplitude and intensity average lifetimes gave similar fits.

Electron Paramagnetic Resonance. EPR data were collected with a Bruker ELEXSYS E580. Samples were packed in Suprasil capillaries under a nitrogen atmosphere. All data were collected at room temperature. Typical experimental conditions were as follows: frequency 9.42 GHz, modulation amplitude 2 G, microwave power 1.985 mW, conversion time 40.96 ms, time constant 0.04 ms, sweep time 83.89 s, sweep width 300 G, and a resolution 2048 points.

Photoluminescence Quantum Yield. The PLQY of the SiNSs was determined by collecting absorbance and photoluminescence spectra of SiNSs dispersed in methanol. Absorbance was collected with a PerkinElmer Lambda 750 with the standard transmission detector, and photoluminescence data were collected with a PerkinElmer LS 55 with an excitation wavelength of 370 nm and

slit widths of 5 nm. PLQY was determined with the following equation, using fluorescein dissolved in methanol as a reference:

$$PLQY_{SiNS} = PLQY_{Ref} \left(\frac{\langle Abs_{Ref}(\lambda) | Exc(\lambda) \rangle}{\langle Abs_{SiNS}(\lambda) | Exc(\lambda) \rangle} \right) \left(\frac{\int Em_{SiNS}(\lambda) d\lambda}{\int Em_{Ref}(\lambda) d\lambda} \right)$$

In the above equation, "PLQY_{Ref}" is the PLQY of the fluorescein reference, "Abs_{Ref}(λ)" is the absorbance spectrum of the fluorescein reference, "Abs_{SiNS}(λ)" is the absorbance spectrum of the SiNS sample, "Em_{Ref}(λ)" is the photoluminescence emission spectrum of the fluorescein reference, "Em_{SiNS}(λ)" is the photoluminescence spectrum of a SiNS sample, "Exc(λ)" is the photoluminescence excitation spectrum, and " λ " is the wavelength. All absorbance values were kept below 0.1 to minimize reabsorption effects. Note that the absorbance and excitation spectra are defined over the same wavelength interval such that

$$\langle Abs_i(\lambda)|Exc(\lambda)\rangle = \sum_{\lambda} Abs_i(\lambda) \times Exc(\lambda)$$

ASSOCIATED CONTENT

5 Supporting Information

The Supporting Information is available free of charge at https://pubs.acs.org/doi/10.1021/acsnano.1c04230.

Powder XRD of CaSi₂, PDF of an isolated single silicane sheet, simulated pXRD of stacks of SiNSs, PDF of siloxene structures, FTIR peak assignment table, azimuthally dependent integrated total X-ray scattering, azimuthally integrated X-ray scattering of annealed samples, 2D total scattering data of annealed samples, SEM images of annealed samples, DFT FTIR spectra of silicane oxides and siloxenes, band structures, DFT FTIR calibration, energetics of oxygen-containing nanosheets, TRPL lifetime fitting parameters, PLQY data (PDF)

GIF files that illustrate the vibrational modes (ZIP)

AUTHOR INFORMATION

Corresponding Authors

Matthew G. Panthani — Department of Chemical and Biological Engineering, Iowa State University, Ames, Iowa 50011, United States; orcid.org/0000-0002-3795-2051; Email: panthani@iastate.edu

Luke T. Roling — Department of Chemical and Biological Engineering, Iowa State University, Ames, Iowa 50011, United States; orcid.org/0000-0001-9742-2573; Email: roling@iastate.edu

Author

Bradley J. Ryan – Department of Chemical and Biological Engineering, Iowa State University, Ames, Iowa 50011, United States; orcid.org/0000-0002-7719-5593

Complete contact information is available at: https://pubs.acs.org/10.1021/acsnano.1c04230

Notes

The authors declare no competing financial interest.

ACKNOWLEDGMENTS

The authors would like to thank Leighanne Gallington (Argonne National Laboratory) for collecting the total X-ray scattering data, Atefe Hadi for sample preparation and useful discussions, Dapeng Jing (Iowa State University) for assistance

with XPS measurements, and Catherine Mullen and Zelig Kopel for useful edits to the manuscript. We wish to thank ISU Chemical Instrumentation Facility staff member Sarah Cady for assistance with data acquisition pertaining to the Elexsys 580 FT-EPR. This work was supported by the Department of Defense (DoD) Air Force Office of Scientific Research (AFOSR); initial studies of the optical properties began under the Young Investigator Program (FA9550-17-1-0170) and continued under award number FA9550-20-1-0018. Structural characterization using pair distribution function analysis was supported by the National Science Foundation (DMR 1847370) Early CAREER Development Award. DFT calculations were performed by using supercomputing resources at the Department of Defense (DoD) High Performance Computing Modernization Program: the U.S. Air Force Research Laboratory DoD Supercomputing Resource Center (AFRL DSRC), and the Navy DoD Supercomputing Resource Center (Navy DSRC). The research reported in this paper is partially supported by the HPC@ISU equipment at Iowa State University, some of which has been purchased through funding provided by NSF under MRI grant number CNS 1726447. Use of the Advanced Photon Source at Argonne National Laboratory was supported by the U.S. Department of Energy, Office of Science, Office of Basic Energy Sciences, under Contract No. DE-AC02-06CH11357. All PDF measurements were obtained through the rapid access mail-in program. B.J.R. also acknowledges support from the National Science Foundation Graduate Research Fellowship Program under DGE 1744592. Any opinions, findings, and conclusions or recommendations expressed in this material are those of the authors and do not necessarily reflect the views of the National Science Foundation or the United States Department of Defense.

REFERENCES

- (1) Lukman, S.; Ding, L.; Xu, L.; Tao, Y.; Riis-Jensen, A. C.; Zhang, G.; Wu, Q. Y. S.; Yang, M.; Luo, S.; Hsu, C.; Yao, L.; Liang, G.; Lin, H.; Zhang, Y. W.; Thygesen, K. S.; Wang, Q. J.; Feng, Y.; Teng, J. High Oscillator Strength Interlayer Excitons in Two-Dimensional Heterostructures for Mid-Infrared Photodetection. *Nat. Nanotechnol.* **2020**, *15*, 675–682.
- (2) Ohashi, M.; Shirai, S.; Nakano, H. Direct Chemical Synthesis of Benzyl-Modified Silicane from Calcium Disilicide. *Chem. Mater.* **2019**, 31, 4720–4725.
- (3) Ohshita, J.; Yamamoto, K.; Tanaka, D.; Nakashima, M.; Kunugi, Y.; Ohashi, M.; Nakano, H. Preparation and Photocurrent Generation of Silicon Nanosheets with Aromatic Substituents on the Surface. *J. Phys. Chem. C* **2016**, *120*, 10991–10996.
- (4) Imagawa, H.; Itahara, H. Stabilized Lithium-Ion Battery Anode Performance by Calcium-Bridging of Two Dimensional Siloxene Layers. *Dalton Trans.* **2017**, *46*, 3655–3660.
- (5) Fu, R.; Li, Y.; Wu, Y.; Shen, C.; Fan, C.; Liu, Z. Controlling Siloxene Oxidization to Tailor SiOx Anodes for High Performance Lithium Ion Batteries. *J. Power Sources* **2019**, 432, 65–72.
- (6) Kumai, Y.; Nakano, H. Characteristics of Layered Polysilane and Its Application to Lithium Ion Battery Anodes. *Jpn. J. Appl. Phys.* **2015**, *54*, No. 035201.
- (7) Liu, J.; Yang, Y.; Lyu, P.; Nachtigall, P.; Xu, Y. Few-Layer Silicene Nanosheets with Superior Lithium-Storage Properties. *Adv. Mater.* **2018**, *0*, 1800838.
- (8) Liang, C.; Gu, H.; Xia, Y.; Wang, Z.; Liu, X.; Xia, J.; Zuo, S.; Hu, Y.; Gao, X.; Hui, W.; Chao, L.; Niu, T.; Fang, M.; Lu, H.; Dong, H.; Yu, H.; Chen, S.; Ran, X.; Song, L.; Li, B.; et al. Two-Dimensional Ruddlesden-Popper Layered Perovskite Solar Cells Based on Phase-Pure Thin Films. *Nat. Energy* **2021**, *6*, 1–8.

- (9) Andrei, E. Y.; MacDonald, A. H. Graphene Bilayers with a Twist. *Nat. Mater.* **2020**, *19*, 1265–1275.
- (10) Jin, C.; Tao, Z.; Kang, K.; Watanabe, K.; Taniguchi, T.; Mak, K. F.; Shan, J. Imaging and Control of Critical Fluctuations in Two-Dimensional Magnets. *Nat. Mater.* **2020**, *19*, 1290–1294.
- (11) Wang, L.; Shih, E. M.; Ghiotto, A.; Xian, L.; Rhodes, D. A.; Tan, C.; Claassen, M.; Kennes, D. M.; Bai, Y.; Kim, B.; Watanabe, K.; Taniguchi, T.; Zhu, X.; Hone, J.; Rubio, A.; Pasupathy, A. N.; Dean, C. R. Correlated Electronic Phases in Twisted Bilayer Transition Metal Dichalcogenides. *Nat. Mater.* **2020**, *19*, 861–866.
- (12) Ryan, B. J.; Hanrahan, M. P.; Wang, Y.; Ramesh, U.; Nyamekye, C. K. A.; Nelson, R. D.; Liu, Z.; Huang, C.; Whitehead, B.; Wang, J.; Roling, L. T.; Smith, E. A.; Rossini, A. J.; Panthani, M. G. Silicene, Siloxene, or Silicane? Revealing the Structure and Optical Properties of Silicon Nanosheets Derived from Calcium Disilicide. *Chem. Mater.* **2020**, *32*, 795–804.
- (13) Li, C. H.; van 't Erve, O. M. J.; Jonker, B. T. Electrical Injection and Detection of Spin Accumulation in Silicon at 500 K with Magnetic Metal/Silicon Dioxide Contacts. *Nat. Commun.* **2011**, *2*, 245.
- (14) Ayes, A.; Maskay, A.; Cunha, M. P. da. Predicted and Measured Temperature Compensated Surface Acoustic Wave Devices for High-Temperature Applications. *Electron. Lett.* **2017**, *53*, 699–700.
- (15) Billinge, S. J. L. The Rise of the X-Ray Atomic Pair Distribution Function Method: A Series of Fortunate Events. *Philos. Trans. R. Soc., A* **2019**, 377, 20180413.
- (16) Hunter, K. I.; Bedford, N.; Schramke, K.; Kortshagen, U. R. Probing Dopant Locations in Silicon Nanocrystals *via* High Energy X-Ray Diffraction and Reverse Monte Carlo Simulation. *Nano Lett.* **2020**, *20*, 852–859.
- (17) Petkov, V.; Hessel, C. M.; Ovtchinnikoff, J.; Guillaussier, A.; Korgel, B. A.; Liu, X.; Giordano, C. Structure–Properties Correlation in Si Nanoparticles by Total Scattering and Computer Simulations. *Chem. Mater.* **2013**, 25, 2365–2371.
- (18) Rohani, P.; Banerjee, S.; Sharifi-Asl, S.; Malekzadeh, M.; Shahbazian-Yassar, R.; Billinge, S. J. L.; Swihart, M. T. Synthesis and Properties of Plasmonic Boron-Hyperdoped Silicon Nanoparticles. *Adv. Funct. Mater.* **2019**, 29, 1807788.
- (19) Rietveld, H. M. A Profile Refinement Method for Nuclear and Magnetic Structures. *J. Appl. Crystallogr.* **1969**, *2*, 65–71.
- (20) Billinge, S. J. L. Nanoscale Structural Order from the Atomic Pair Distribution Function (PDF): There's Plenty of Room in the Middle. *J. Solid State Chem.* **2008**, *181*, 1695–1700.
- (21) Castillo, S. M.; Tang, Z.; Litvinchuk, A. P.; Guloy, A. M. Lattice Dynamics of the Rhombohedral Polymorphs of CaSi₂. *Inorg. Chem.* **2016**, *55*, 10203–10207.
- (22) Nedumkandathil, R.; Benson, D. E.; Grins, J.; Spektor, K.; Häussermann, U. The 3R Polymorph of CaSi₂. *J. Solid State Chem.* **2015**, 222, 18–24.
- (23) Cultrara, N. D.; Wang, Y.; Arguilla, M. Q.; Scudder, M. R.; Jiang, S.; Windl, W.; Bobev, S.; Goldberger, J. E. Synthesis of 1T, 2H, and 6R Germanane Polytypes. *Chem. Mater.* **2018**, *30*, 1335–1343.
- (24) Holder, C. F.; Schaak, R. E. Tutorial on Powder X-Ray Diffraction for Characterizing Nanoscale Materials. *ACS Nano* **2019**, 13, 7359–7365.
- (25) Kautsky, H. Über Einige Ungesättigte Siliciumverbindungen. Z. Für Anorg. Allg. Chem. 1921, 117, 209–242.
- (26) Kautsky, H.; Vogell, W.; Oeters, F. Notizen: Die Bedeutung Elektronenmikroskopischer Untersuchungen Für Die Konstitutions-Und Strukturaufklärung Des Siloxens. Z. Naturforsch., B: J. Chem. Sci. 1955, 10, 597–598.
- (27) Beekman, M.; Kauzlarich, S. M.; Doherty, L.; Nolas, G. S. Zintl Phases as Reactive Precursors for Synthesis of Novel Silicon and Germanium-Based Materials. *Materials* **2019**, *12*, 1139.
- (28) Yamanaka, S.; Matsu-ura, H.; Ishikawa, M. New Deintercalation Reaction of Calcium from Calcium Disilicide. Synthesis of Layered Polysilane. *Mater. Res. Bull.* **1996**, *31*, 307–316.

- (29) Paul, W.; Anderson, D. A. Properties of Amorphous Hydrogenated Silicon, with Special Emphasis on Preparation by Sputtering. *Sol. Energy Mater.* **1981**, 5 (3), 229–316.
- (30) Chittick, R. C.; Alexander, J. H.; Sterling, H. F. The Preparation and Properties of Amorphous Silicon. J. Electrochem. Soc. 1969, 116, 77.
- (31) Sai, H.; Matsui, T.; Matsubara, K. Stabilized 14.0%-Efficient Triple-Junction Thin-Film Silicon Solar Cell. *Appl. Phys. Lett.* **2016**, *109*, 183506.
- (32) Jiang, S.; Bianco, E.; Goldberger, J. E. The Structure and Amorphization of Germanane. J. Mater. Chem. C 2014, 2, 3185–3188.
- (33) Harris, J. T.; Hueso, J. L.; Korgel, B. A. Hydrogenated Amorphous Silicon (a-Si:H) Colloids. *Chem. Mater.* **2010**, 22, 6378–6383.
- (34) Ubara, H.; Imura, T.; Hiraki, A.; Hirabayashi, I.; Morigaki, K. Structural Change from Crystalline to Amorphous States in Siloxene by Thermal Annealing. *J. Non-Cryst. Solids* **1983**, 59–60, 641–644.
- (35) Holmes, J. D.; Johnston, K. P.; Doty, R. C.; Korgel, B. A. Control of Thickness and Orientation of Solution-Grown Silicon Nanowires. *Science* **2000**, 287, 1471–1473.
- (36) Lee, B. G.; Luo, J. W.; Neale, N. R.; Beard, M. C.; Hiller, D.; Zacharias, M.; Stradins, P.; Zunger, A. Quasi-Direct Optical Transitions in Silicon Nanocrystals with Intensity Exceeding the Bulk. *Nano Lett.* **2016**, *16*, 1583–1589.
- (37) Lagorio, M. G. Determination of Fluorescence Quantum Yields in Scattering Media. *Methods Appl. Fluoresc.* **2020**, *8*, No. 043001.
- (38) Pankove, J. I.; Carlson, D. E. Photoluminescence of Hydrogenated Amorphous Silicon. *Appl. Phys. Lett.* **1977**, *31*, 450–451.
- (39) Sidhu, L. S.; Kosteski, T.; Zukotynski, S.; Kherani, N. P.; Shmayda, W. T. Effect of Dangling-Bond Density on Luminescence in Tritiated Amorphous Silicon. *Appl. Phys. Lett.* **1999**, *74*, 3975–3977.
- (40) Lannoo, M.; Delerue, C.; Allan, G. Nonradiative Recombination on Dangling Bonds in Silicon Crystallites. *J. Lumin.* **1993**, *57*, 243–247.
- (41) He, J.; Tse, J. S.; Klug, D. D.; Preston, K. F. Layered Polysilane: Thermolysis and Photoluminescence. *J. Mater. Chem.* **1998**, *8*, 705–710.
- (42) Toby, B. H.; Von Dreele, R. B. GSAS-II: The Genesis of a Modern Open-Source All Purpose Crystallography Software Package. *J. Appl. Crystallogr.* **2013**, *46*, 544–549.
- (43) Qiu, X.; Thompson, J. W.; Billinge, S. J. L. PDFgetX2: A GUI-Driven Program to Obtain the Pair Distribution Function from X-Ray Powder Diffraction Data. *J. Appl. Crystallogr.* **2004**, *37*, 678–678.
- (44) Farrow, C. L.; Juhas, P.; Liu, J. W.; Bryndin, D.; Božin, E. S.; Bloch, J.; Proffen, T.; Billinge, S. J. L. PDFfit2 and PDFgui: Computer Programs for Studying Nanostructure in Crystals. *J. Phys.: Condens. Matter* **2007**, *19*, 335219.
- (45) Deringer, V. L.; Bernstein, N.; Bartók, A. P.; Cliffe, M. J.; Kerber, R. N.; Marbella, L. E.; Grey, C. P.; Elliott, S. R.; Csányi, G. Realistic Atomistic Structure of Amorphous Silicon from Machine-Learning-Driven Molecular Dynamics. *J. Phys. Chem. Lett.* **2018**, *9*, 2879–2885.
- (46) Kresse, G.; Furthmüller, J. Efficient Iterative Schemes for *ab Initio* Total-Energy Calculations Using a Plane-Wave Basis Set. *Phys. Rev. B: Condens. Matter Mater. Phys.* **1996**, *54*, 11169–11186.
- (47) Kresse, G.; Furthmüller, J. Efficiency of *ab Initio* Total Energy Calculations for Metals and Semiconductors Using a Plane-Wave Basis Set. *Comput. Mater. Sci.* **1996**, *6*, 15–50.
- (48) Perdew, J. P.; Burke, K.; Ernzerhof, M. Generalized Gradient Approximation Made Simple. *Phys. Rev. Lett.* **1996**, *77*, 3865–3868.
- (49) Kresse, G.; Joubert, D. From Ultrasoft Pseudopotentials to the Projector Augmented-Wave Method. *Phys. Rev. B: Condens. Matter Mater. Phys.* 1999, 59, 1758–1775.
- (50) Blöchl, P. E. Projector Augmented-Wave Method. *Phys. Rev. B: Condens. Matter Mater. Phys.* **1994**, *50*, 17953–17979.
- (51) Monkhorst, H. J.; Pack, J. D. Special Points for Brillouin-Zone Integrations. *Phys. Rev. B* **1976**, *13*, 5188–5192.

- (52) Esfarjani, K.; Hashi, Y.; Onoe, J.; Takeuchi, K.; Kawazoe, Y. Vibrational Modes and IR Analysis of Neutral Photopolymerized C₆₀ Dimers. *Phys. Rev. B: Condens. Matter Mater. Phys.* **1998**, *57*, 223–229
- (53) Karhánek, D.; Bučko, T.; Hafner, J. A Density-Functional Study of the Adsorption of Methane-Thiol on the (111) Surfaces of the Ni-Group Metals: II. Vibrational Spectroscopy. *J. Phys.: Condens. Matter* **2010**, 22, 265006.
- (54) Karhánek, D. Self-Assembled Monolayers Studied by Density-Functional Theory. Ph.D. Dissertation, Universität Wien, Vienna, Austria, 2010.
- (55) Baroni, S.; de Gironcoli, S.; Dal Corso, A.; Giannozzi, P. Phonons and Related Crystal Properties from Density-Functional Perturbation Theory. *Rev. Mod. Phys.* **2001**, *73*, 515–562.
- (56) Giannozzi, P.; Baroni, S. Vibrational and Dielectric Properties of C_{60} from Density-Functional Perturbation Theory. *J. Chem. Phys.* **1994**, *100*, 8537–8539.
- (57) Karhánek, D. Calculation of Vibrational (IR) Intensities, https://homepage.univie.ac.at/david.karhanek/downloads.html (accessed Sep 18, 2017).
- (58) Sillen, A.; Engelborghs, Y. The Correct Use of "Average" Fluorescence Parameters. *Photochem. Photobiol.* **1998**, *67*, 475–486.